

# Boosting the Cycling Stability of Manganese Prussian Blue Analogs by Cu-Substitution and Water Reduction for Sodium-Ion Batteries

Yuting Gao, Jie Li, Youchen Hao, Yao Huang, Weiwei Zha, Xiaoliang Zhou, and Yinzhu Jiang\*

Manganese-based Prussian blue analog (MnPBA) shows great potential as a high energy density and low-cost cathode material for sodium-ion batteries (SIBs) due to its electrochemical activity, high redox potential, low-cost raw materials, and facile synthesis. However, its practical application is severely challenged by the high water content (>10 wt%) in the framework and the Jahn-Teller effect from high-spin Mn<sup>3+</sup>, leading to poor reversibility and rapid capacity decay during cycling. Herein, Cu-substituted MnPBA samples (CuMnPBAs) are successfully synthesized under

high-concentration chelation conditions, which reduced the water content and alleviated the Jahn-Teller effect from Mn<sup>3+</sup>. Accordingly, the optimal 25% Cu-substituted MnPBA (CuMnPBA-25) exhibits a significantly reduced water content of 7.6% and excellent cyclability, maintaining 81.2 mAh g<sup>-1</sup> at 1 C after 700 cycles. Furthermore, the CuMnPBA-25/hard carbon (HC) pouch cell exhibits superb capacity retention of 80.9% after 280 cycles. This research provides new insights into the development of highly stable PBAs for practical applications in SIBs.

## 1. Introduction

Developing energy storage systems is critical for advancing renewable energy in response to escalating environmental challenges.<sup>[1,2]</sup> Sodium-ion batteries (SIBs), based on the abundant and low-cost sodium resources, are becoming one of the most promising complements to lithium-ion batteries in light of the increasing demands for energy storage.<sup>[3–5]</sup> Among various

cathode materials for SIBs, Prussian blue analogs (PBAs) stand out as promising candidates for commercialization owing to their 3D open framework, abundant redox-active sites, and facile synthesis.<sup>[6–10]</sup> In particular, the manganese-based Prussian blue analog (MnPBA), which combines high redox potential with high theoretical capacity, has attracted significant attention.<sup>[11]</sup> However, the high water content in the MnPBA framework and the Jahn-Teller effect associated with high-spin Mn<sup>3+</sup> leads to rapid capacity fading upon cycling.<sup>[12–14]</sup>

Elemental substitution is widely accepted as a feasible strategy for reducing water content and stabilizing the cyclability of PBAs.<sup>[15,16]</sup> For instance, Liu et al. introduced copper into iron-based PBAs to reduce water content, leading to improved structure stability and enhanced electrochemical performance.<sup>[17]</sup> Similarly, divalent zinc ions with no electrochemical activity were introduced into MnPBA to minimize structural destruction and improve cycling stability.<sup>[18]</sup> Although elemental substitution can reduce water content and stabilize the structure of PBAs, preparing low-water PBAs with excellent cycling performance remains challenging.<sup>[19–21]</sup> In our previous work, a high-concentration chelating agent effectively controlled the coprecipitation processes to obtain low-water PBAs.<sup>[22]</sup> Therefore, the dual strategy of using a high-concentration chelating agent and Cu-substitution could be advantageous for synthesizing low-water and high-stability MnPBA.

Herein, micro-scale CuMnPBAs were synthesized using a dual strategy of high-concentration chelating and Cu-substitution, significantly reducing the water content and improving the cycling stability of MnPBA. The optimal 25% Cu-substituted MnPBA (CuMnPBA-25) was achieved with a notably reduced water content of 7.6%, exhibiting a high reversible capacity of 119.4 mAh g<sup>-1</sup> at 0.5 C and demonstrating excellent capacity retention of 72.4% after 700 cycles. In situ X-ray diffraction

Y. Gao, Y. Huang, Y. Jiang

School of Materials Science and Engineering

Zhejiang University

Hangzhou 310058, China

E-mail: yzjiang@zju.edu.cn

Y. Gao

College of Quality and Standardization

China Jiliang University

Hangzhou 310018, China

J. Li, X. Zhou

College of Chemistry and Chemical Engineering

Southwest Petroleum University

Chengdu 610500, China

Y. Hao, Y. Jiang

ZJU-Hangzhou Global Scientific and Technological Innovation Center

Zhejiang University

Hangzhou 311215, China

W. Zha

Cell Development Department

Huzhou Horizontal Na Energy Technology Co., Ltd.

Huzhou 313000, China

Y. Jiang

State Key Laboratory of Baiyunobo Rare Earth Resource Researches and

Comprehensive Utilization

Baotou Research Institute of Rare Earths

Baotou 014030, China



Supporting information for this article is available on the WWW under <https://doi.org/10.1002/batt.202500216>

(XRD) indicated that CuMnPBA-25 exhibits highly reversible phase transition during the charge–discharge process. Furthermore, the kilogram-scale synthesis of CuMnPBA-25 and the successful assembly of CuMnPBA-25/hard carbon (HC) pouch cells with outstanding cycling performance further confirm its practicality for large-scale commercial applications.

## 2. Results and Discussion

### 2.1. Morphological and Structural Characterization

A facile chelating-assisted coprecipitation method was employed to synthesize MnPBA and CuMnPBA. Their microscopic morphologies and fine phase structures were analyzed using scanning electron microscope (SEM) and transmission electron microscope (TEM). SEM images reveal that MnPBA and CuMnPBA-25 exhibit cubic block and polyhedron-like morphologies (Figure 1a,b1), respectively, with sizes of approximately 10  $\mu\text{m}$ . The TEM images (Figure 1a2,b2) reveal that the single particle sizes of MnPBA and CuMnPBA-25 range from 10 to 20  $\mu\text{m}$ . The high-resolution transmission electron microscopy (HRTEM) images (Figure 1a3,b3) and selected area electron diffraction (SAED) further confirm the structure of the as-prepared samples (Figure 1a4,b4). For MnPBA and CuMnPBA-25, the well-defined lattice fringes with interplanar spacings in the (200) and (211) planes are 5.23 and 3.66  $\text{\AA}$ , 5.25 and 3.67  $\text{\AA}$ , respectively, indicating that both samples exhibit a monoclinic phase structure. Furthermore, the elements in CuMnPBA-25 exhibit a uniform distribution of C, N, Na, Fe, Cu, and Mn, as shown in Figure 1c. In addition, the 10% Cu-substituted MnPBA (CuMnPBA-10) exhibits a polyhedron-like morphology, while the 90% Cu-substituted MnPBA (CuMnPBA-90) displays a lamellar structure, as shown in Figure S1a–c (Supporting Information). The copper Prussian blue analog (CuPBA) shows a lamellar morphology with a higher specific surface area (Figure S1d and S2, Supporting Information).

To investigate the structural changes of the as-prepared samples, Rietveld refinement XRD was performed on CuPBA, CuMnPBA-25, and MnPBA, as shown in Figure 2a–c. The corresponding lattice parameters are detailed in Table S1–S3 (Supporting Information). Obviously, Cu substitution increases the occupancy of Na sites, which may be related to the reduction in water content.<sup>[23]</sup> Furthermore, the crystal structures of the other CuMnPBA were investigated by XRD, as shown in Figure S3 (Supporting Information). The results revealed that all samples exhibit a monoclinic structure with the P2<sub>1</sub>/n space. For the 75% Cu-substituted MnPBA (CuMnPBA-75), the (400)/(022) crystal planes merged into a (400) crystal plane, indicating a reduction in structural distortion. Moreover, with the increase of Cu substitution, CuMnPBA-90 exhibited strong peaks corresponding to CuPBA and weak peaks associated with MnPBA. This may be attributed to the significant differences in lattice parameters between CuPBA and MnPBA.<sup>[24]</sup>

The chemical structures of CuPBA, CuMnPBA-25, and MnPBA were analyzed using Raman spectroscopy and Fourier transform infrared spectroscopy (FTIR), as shown in Figure 2d,e. The as-prepared samples exhibited two  $\nu(\text{CN})$  bands at 2086 and 2124  $\text{cm}^{-1}$  in the Raman spectra, confirming the presence of  $\text{Fe}(\text{CN})_6^{4-}$  groups.<sup>[17]</sup> In addition, the main absorption peaks of CuPBA appear at 2061 and 2105  $\text{cm}^{-1}$  in the FTIR spectra, corresponding to the stretching vibrations of  $\text{C}\equiv\text{N}$ . For CuMnPBA-25 and MnPBA, the main stretching vibration peaks of  $\text{C}\equiv\text{N}$  were observed at 2064 and 2053  $\text{cm}^{-1}$ , respectively. This similarity in absorption peaks suggests that the crystal structure of CuMnPBA-25 closely resembles that of MnPBA.<sup>[25]</sup> Notably, the intensity of the O–H peak at 1619  $\text{cm}^{-1}$  is reduced in CuMnPBA-25 compared to MnPBA, indicating that the Cu substitution strategy effectively decreases water content.

Thermogravimetric analysis (TGA) was conducted to determine the water content of the as-prepared samples, as shown in Figure 2f and Figure S4 (Supporting Information). The weight loss observed below 100 °C, between 100 and 180 °C, and

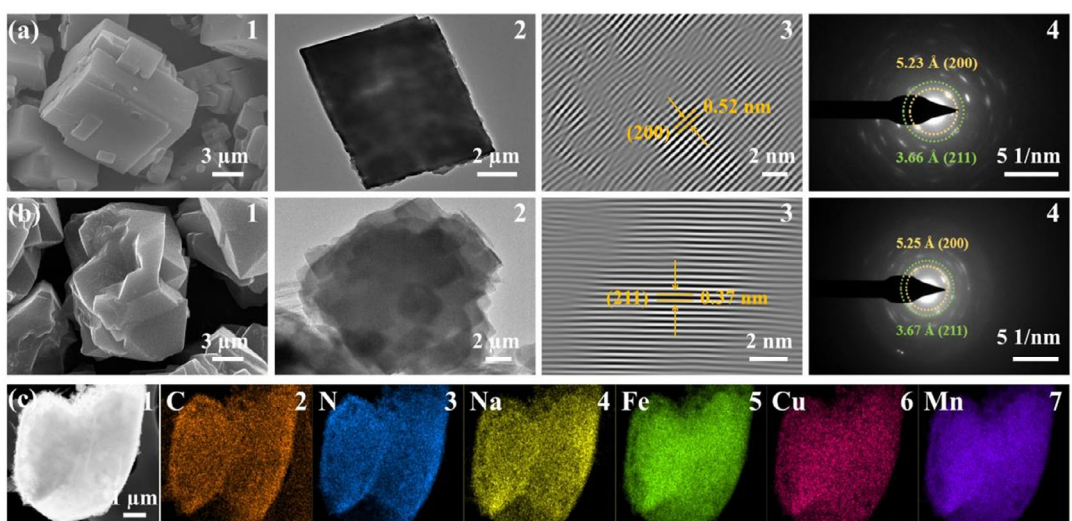


**Figure 1.** Morphological characterization: 1) SEM, 2) TEM, 3) HRTEM, and 4) HAADF-STEM with 5 1/nm SAED patterns of a) MnPBA and b) CuMnPBA-25. c1) The dark-field HAADF images and c2–c7) corresponding elemental mappings.

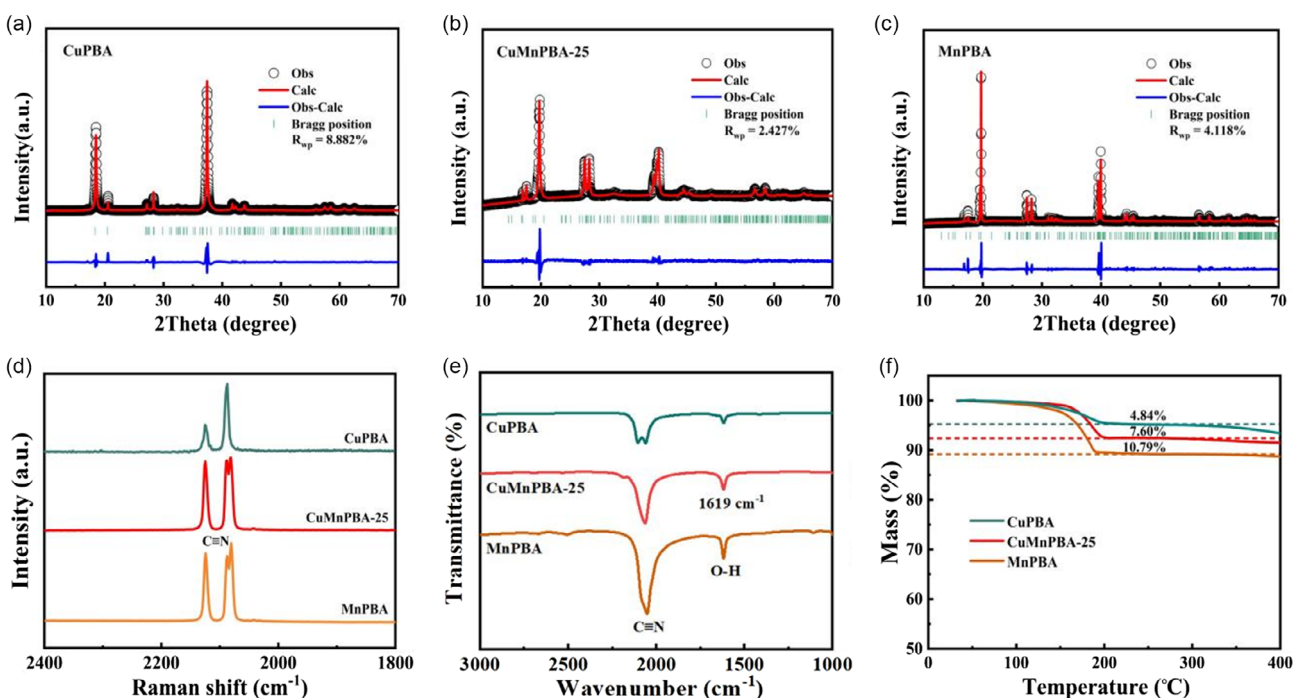


**Figure 2.** Rietveld refinements of a) CuPBA, b) CuMnPBA-25, and c) MnPBA. d) Raman spectra, e) FTIR curves, and f) TGA curves of the as-prepared samples.

180–250 °C was attributed to adsorbed water, interstitial water, and coordinated water, respectively.<sup>[26]</sup> Specifically, interstitial water constituted the majority of the water content in the samples. Upon heating to 250 °C, CuPBA, CuMnPBA-90, CuMnPBA-75, CuMnPBA-25, CuMnPBA-10, and MnPBA exhibited weight losses of 4.84%, 4.91%, 7.25%, 7.6%, 8.27%, and 10.79%, respectively, indicating that CuMnPBA-25 has lower interstitial water than MnPBA after Cu substitution. Importantly, CuMnPBA-25 showed no significant weight loss between 250 and 400 °C, suggesting superior stability at high temperatures. Furthermore, the elemental composition and chemical formulas of the synthesized samples were characterized using inductively coupled plasma optical emission spectrometer (ICP-OES) and elemental analysis (EA), with results summarized in Table S4 and S5 (Supporting Information).

## 2.2. Electrochemical Performance and Mechanisms

The electrochemical behaviors of CuPBA, CuMnPBA-25, and MnPBA were analyzed using cyclic voltammetry (CV) within a voltage range of 2.0–4.2 V. As illustrated in Figure 3a–c, the redox peak potentials of all three samples shift correspondingly with changes in scan rate, with CuPBA exhibiting a lower potential difference at scan rates ranging from 0.1 to 0.6 mV s<sup>-1</sup>. CuMnPBA-25 exhibited redox behavior similar to MnPBA, with anodic and cathodic peaks at 3.62/3.69 V and 3.22/3.27 V (0.6 mV s<sup>-1</sup>), respectively, which can be attributed to the Mn<sup>3+</sup>/Mn<sup>2+</sup> and Fe<sup>3+</sup>/Fe<sup>2+</sup> redox couples.<sup>[27]</sup> Notably, the voltage polarization of CuMnPBA-25 is lower than that of MnPBA, which might be attributed to the reduced water content in the framework after Cu substitution.<sup>[28]</sup>

The electrochemical performance of CuMnPBA was investigated by galvanostatic charge-discharge, as shown in Figure 3d and Figure S5a (Supporting Information). Specifically, CuMnPBA-10, CuMnPBA-25, CuMnPBA-75, and CuMnPBA-90 exhibited reversible capacities of 139.6, 119.4, 103.5, and 98.5 mAh g<sup>-1</sup> at 0.5 C (1 C = 100 mA g<sup>-1</sup>), respectively. CuPBA and CuMnPBA-90 show a single voltage plateau at 3.5 V during the initial charge, indicating activation of only the Fe<sub>LS</sub><sup>3+/2+</sup> redox couple.<sup>[29]</sup> During discharge, two voltage plateaus appeared at 3.17/3.40 and 2.65/2.75 V, indicating the activation of both the Cu<sub>HS</sub><sup>2+/+</sup> and Fe<sub>LS</sub><sup>3+/2+</sup> redox couples in the reaction. With increasing Cu substitution, the voltage plateau at 3.70–3.85 V continuously shortens, corresponding to the Mn<sub>HS</sub><sup>3+/2+</sup>.<sup>[30,31]</sup> In addition, the long-term cycling performance of CuMnPBA was evaluated at 1 C, as illustrated in Figure 3e and Figure S5b (Supporting Information). Specifically, CuPBA, CuMnPBA-10, CuMnPBA-25, CuMnPBA-75, CuMnPBA-90, and MnPBA exhibited capacity retentions of 87.7%, 77.7%, 88.5%, 82.9%, 61.2%, and 57.2% after 100 cycles, respectively. Notably, CuMnPBA-25 shows remarkable capacity retention of 72.4% after 700 cycles, outperforming MnPBA (26.1% after 480 cycles). Figure S6 (Supporting Information) reveals that CuMnPBA-25 exhibits the highest energy density (305 Wh kg<sup>-1</sup>) after the long cycles. Figure 3f illustrates the rate performance of CuPBA, CuMnPBA-25, and MnPBA at different current densities, with CuMnPBA-25 demonstrating superior capacity retention at 5 C (58.1%) compared to MnPBA (46.3%).

To further determine the electrode reaction kinetics, the as-prepared samples were analyzed using electrochemical impedance spectroscopy (EIS), as shown in Figure 3g. The fitting results from the equivalent circuit indicate that CuPBA, CuMnPBA-25, and MnPBA have charge transfer resistances ( $R_{ct}$ ) of 224, 548,

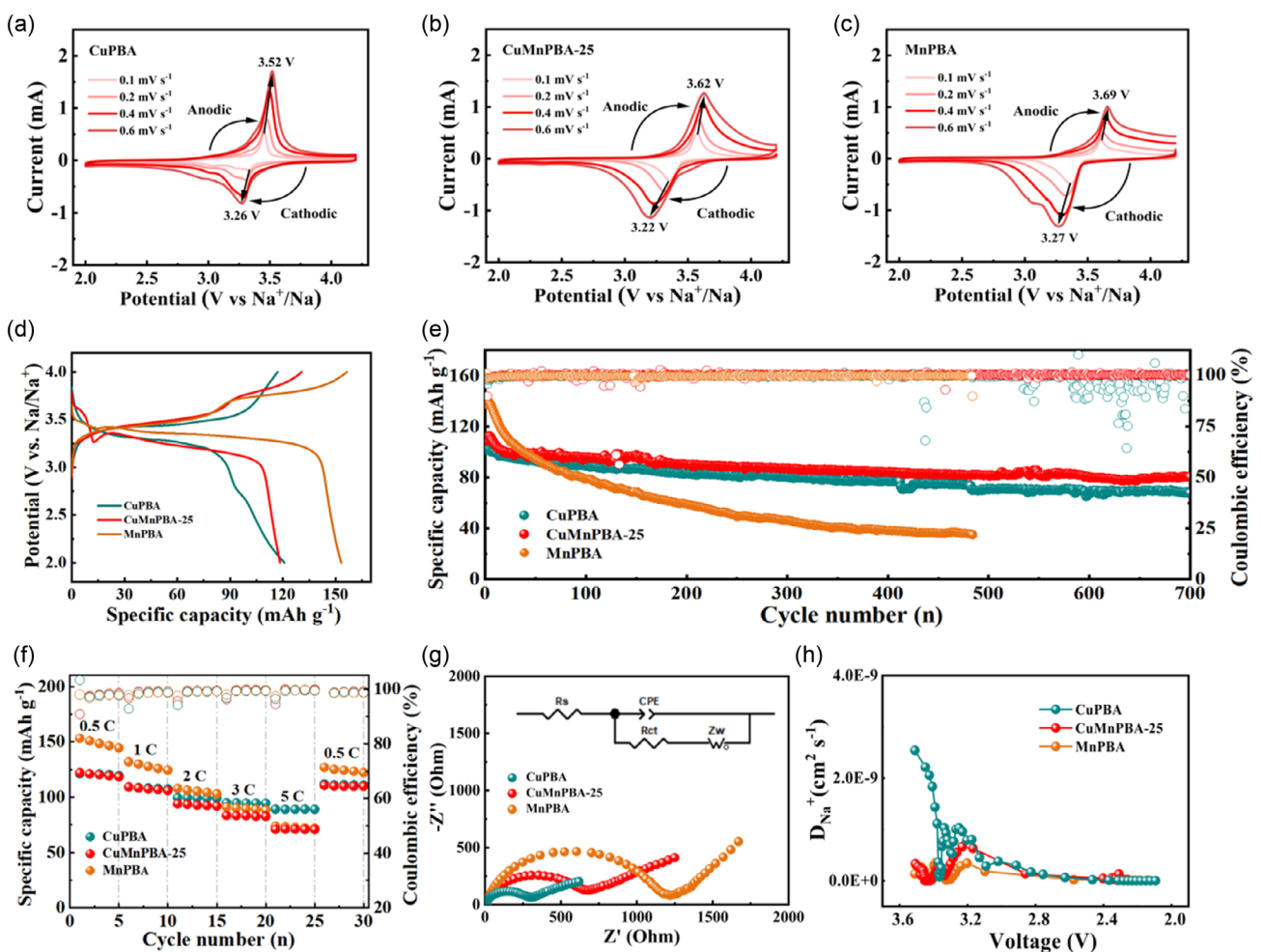


**Figure 3.** Electrochemical performance of PBAs electrodes: CV curves of a) CuPBA, b) CuMnPBA-25, and c) MnPBA at different scan rates. d) The initial charge–discharge curves and e) cycling performance of the as-prepared samples. f) Rate capability, g) EIS spectra, and h) calculated Na<sup>+</sup> diffusion coefficients of CuPBA, CuMnPBA-25, and MnPBA.

and 1073 Ω, respectively. This suggests that CuMnPBA-25 exhibits faster Na<sup>+</sup> ions intercalation/deintercalation kinetics compared to MnPBA. Furthermore, the Na<sup>+</sup> diffusion coefficient ( $D_{\text{Na}^+}$ ) was determined using the galvanostatic intermittent titration technique (GITT), as depicted in Figure 3h. The  $D_{\text{Na}^+}$  values for the three samples were calculated using the following Equation (1):

$$D_{\text{Na}^+} = \frac{4}{\pi \tau} \left( \frac{m_b V_M}{M_b S} \right)^2 \left( \frac{\Delta E_s}{\Delta E_t} \right)^2 (\text{cm}^2 \text{s}^{-1}) \quad (1)$$

Notably, compared with MnPBA ( $5.96 \times 10^{-14} - 3.51 \times 10^{-10} \text{ cm}^2 \text{s}^{-1}$ ), the  $D_{\text{Na}^+}$  values of CuMnPBA-25 ( $1.40 \times 10^{-11} - 2.54 \times 10^{-9} \text{ cm}^2 \text{s}^{-1}$ ) significantly increase during discharging. This indicates that the Na<sup>+</sup> ion diffusion kinetics of CuMnPBA-25 have improved, which can be attributed to the Cu substitution strategy reducing water content and enhancing the electrode reaction kinetics.

In situ XRD analysis was performed to investigate the structural evolution of CuMnPBA-25 during charging and discharging, with the results depicted in Figure 4a,b. The initial phase of CuMnPBA-25 exhibits a monoclinic structure characterized by distinct peaks located at 19.6° and 19.9°, which are attributed to the

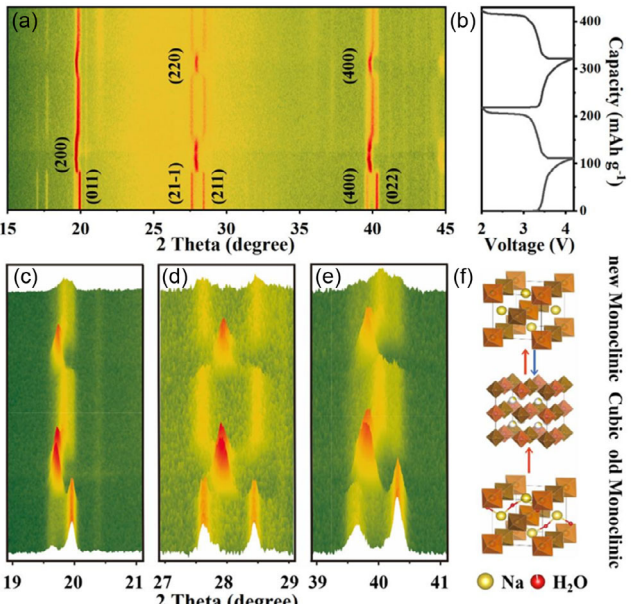


**Figure 4.** a) In situ XRD patterns of CuMnPBA-25 and b) corresponding charge–discharge curves. c–e) Local in situ XRD contour plots of CuMnPBA-25. f) Schematic diagram of the phase transition.

(200) and (011) planes, respectively, along with peaks observed at 27.6° and 28.5°, corresponding to the (21-1) and (211) planes. The peaks at 36.6° and 40.3° are associated with the (400) and (022) planes, respectively. During the charging process, the three pairs of characteristic peaks merged, corresponding to the (200), (220), and (400) planes, respectively. This merging implies a transition from a monoclinic to a cubic structure. During discharging, the (220) and (400) planes split into the (21-1)/(211) and (400)/(022) planes, respectively, indicating the emergence of a new monoclinic structure, as illustrated in Figure 4c-f. Different from the pristine monoclinic structure, the new monoclinic structure does not exhibit a distinct (011) plane, and the (200) plane slightly shifts to higher degrees, suggesting a slight shrinkage in the cell volume. These changes are attributed to the removal of interstitial water from the pristine structure during charging.<sup>[23]</sup> Importantly, CuMnPBA-25 exhibits a highly reversible monoclinic-cubic-monoclinic structure in the second cycle. Notably, the absence of a tetragonal structure during the Na<sup>+</sup> insertion/extraction indicates that Cu substitution effectively suppressed the Jahn-Teller effect. This suppression could be one of the reasons for the significant enhancement in the cyclic performance of CuMnPBA-25.

### 2.3. Practical Applications and Performance of Pouch Cells

The exceptional sodium storage properties of CuMnPBA-25 further highlight its potential for practical applications. Figure 5a illustrates the synthesis process conducted on a kilogram scale in a 50 L reactor, while Figure 5b displays the CuMnPBA-25 powder sample after vacuum drying. Moreover, the particle size distributions of CuPBA, CuMnPBA-25, and MnPBA are shown in Figure S7a-c (Supporting Information). The sharper peak for CuMnPBA-25 suggests a more uniform particle size distribution

compared to MnPBA. It is noteworthy that the tap densities of CuPBA ( $0.34 \text{ g cm}^{-3}$ ) with a lamellar morphology and MnPBA ( $0.81 \text{ g cm}^{-3}$ ) with a cubic block morphology are lower, failing to meet the requirements for commercial application. However, the polyhedron-like CuMnPBA-25 exhibits larger particle sizes and a higher tap density ( $1.06 \text{ g cm}^{-3}$ ), as illustrated in Figure S7d (Supporting Information), which aligns with previous literature reports.<sup>[32]</sup> Furthermore, CuMnPBA-25/HC pouch cells were assembled using CuMnPBA-25 as the cathode and HC as the anode, as depicted in Figure 5c. Figure 5d shows the charge-discharge curves of the CuMnPBA-25/HC pouch cell at different cycles, achieving an initial discharge capacity of  $104.8 \text{ mAh g}^{-1}$  at 1C. The CuMnPBA-25/HC pouch cell maintains a high capacity retention of 80.9% after 280 cycles, as shown in Figure 5e. These results confirm that CuMnPBA-25 exhibits significant potential for practical application in SIBs.

## 3. Conclusions

In summary, we successfully synthesized CuMnPBA-25 under high-concentration chelating agent conditions with Cu substitution, exhibiting low water content and high stability. This dual strategy effectively reduces interstitial water and inhibits Jahn-Teller effect. In situ XRD analysis reveals that CuMnPBA-25 undergoes a reversible monoclinic-cubic-monoclinic phase transition during Na<sup>+</sup> insertion/extraction. Benefiting from these advantages, CuMnPBA-25 achieves an excellent capacity of  $81.2 \text{ mAh g}^{-1}$  at 1C after 700 cycles. To demonstrate the commercial potential of CuMnPBA-25, CuMnPBA-25/HC pouch cells were fabricated, exhibiting stable cyclability with 80.9% capacity retention after 280 cycles. This research provides a rational strategy for enhancing the cycling stability of PBAs in SIBs, paving the

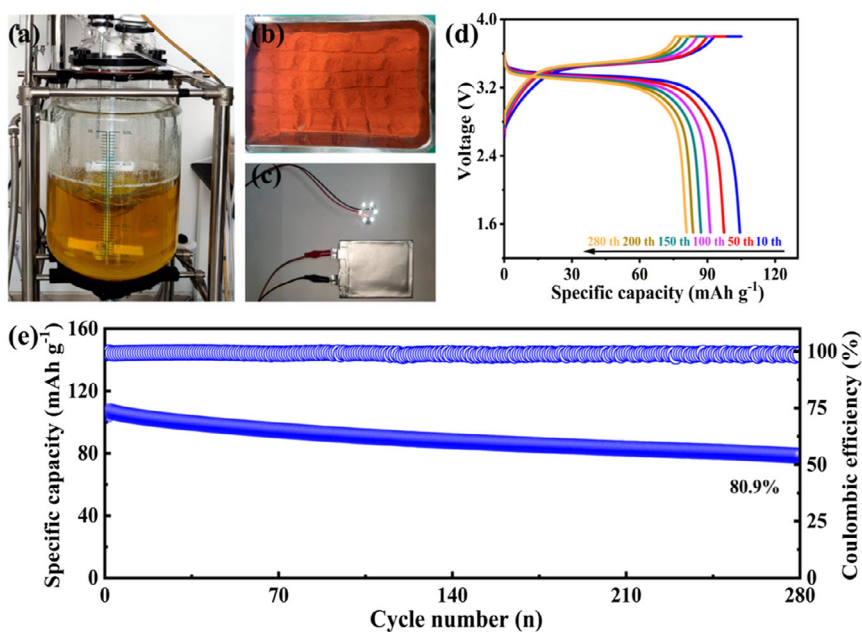


**Figure 5.** a) Large-scale synthesis of CuMnPBA-25 in a 50 L reactor. b) Powder sample of CuMnPBA-25 after vacuum drying. c) Assembling of the CuMnPBA-25/HC pouch cell. d) Charge–discharge curves at different cycles. e) Cycling performance of the CuMnPBA-25/HC pouch cell.

way for their practical application in high-performance rechargeable batteries.

## 4. Experimental Section

Comprehensive details regarding material preparation, characterization, electrochemical measurements, and calculation methodologies can be found in the supplementary information.

## Acknowledgements

This work was supported by the National Key R&D Program (2019YFE0111200), Zhejiang Provincial Natural Science Foundation of China (LZ23B030003), the Fundamental Research Funds for the Central Universities (2021FZZX001-09), and the Science and Technology Projects of China Northern Rare Earth (Group) High-tech Co., Ltd. (BFXT-2022-D-0018).

## Conflict of Interest

The authors declare no conflict of interest.

## Author Contributions

**Yuting Gao:** conceptualization (equal), formal analysis (lead), investigation (lead), methodology (lead), software (lead), supervision (lead), writing—original draft (lead), writing—review and editing (lead). **Jie Li:** investigation (equal), software (equal), writing—review and editing (equal). **Youchen Hao:** investigation (equal), methodology (equal), writing—review and editing (equal). **Yao Huang:** investigation (lead), methodology (lead). **Weiwei Zha:** investigation (equal), supervision (equal). **Xiaoliang Zhou:** methodology (supporting), supervision (supporting). **Yinzhu Jiang:** funding acquisition (lead), supervision (lead), writing—review and editing (equal).

## Data Availability Statement

The data that support the findings of this study are available from the corresponding author upon reasonable request.

**Keywords:** Cu substitution • long cycle life • Prussian blue analogs • sodium-ion batteries

- [1] Y. Luo, Y. Tang, S. Zheng, Y. Yan, H. Xue, H. Pang, *J. Mater. Chem. A* **2018**, *6*, 4236.
- [2] V. Soundharajan, S. Nithiananth, K. Sakthiabirami, J. H. Kim, C.-Y. Su, J.-K. Chang, *J. Mater. Chem. A* **2022**, *10*, 1022.
- [3] K. Turcheniuk, D. Bondarev, V. Singhal, G. Yushin, *Nature* **2018**, *559*, 467.
- [4] E. C. Evarts, *Nature* **2015**, *526*, S93.
- [5] J. B. Goodenough, K.-S. Park, *J. Am. Chem. Soc.* **2013**, *135*, 1167.
- [6] A. Ramesh, A. Tripathi, P. Balaya, *Int. J. Appl. Ceram. Tec.* **2022**, *19*, 913.
- [7] J. Xiao, H. Gao, K. Tang, M. Long, J. Chen, H. Liu, G. Wang, *Small Methods* **2022**, *6*, 2101292.
- [8] Y. Mizuno, M. Okubo, E. Hosono, T. Kudo, H. Zhou, K. Ohishi, *J. Phys. Chem. C* **2013**, *117*, 10877.
- [9] W. Wang, Z. Hu, Z. Yan, J. Peng, M. Chen, W. Lai, Q.-F. Gu, S.-L. Chou, H.-K. Liu, S.-X. Dou, *Energy Storage Mater.* **2020**, *30*, 42.
- [10] W. Wang, Y. Gang, Z. Hu, Z. Yan, W. Li, Y. Li, Q.-F. Gu, Z. Wang, S.-L. Chou, H.-K. Liu, S.-X. Dou, *Nat. Commun.* **2020**, *11*, 980.
- [11] X.-H. Ma, W. Jia, J. Wang, J.-H. Zhou, Y.-D. Wu, Y.-Y. Wei, Z.-F. Zi, J.-M. Dai, *Ceram. Int.* **2019**, *45*, 740.
- [12] J. Song, L. Wang, Y. Lu, J. Liu, B. Guo, P. Xiao, J.-J. Lee, X.-Q. Yang, G. Henkelman, J. B. Goodenough, *J. Am. Chem. Soc.* **2015**, *137*, 2658.
- [13] L. Jiang, Y. Lu, C. Zhao, L. Liu, J. Zhang, Q. Zhang, X. Shen, J. Zhao, X. Yu, H. Li, X. Huang, L. Chen, Y.-S. Hu, *Nat. Energy* **2019**, *4*, 495.
- [14] Y. Shang, X. Li, J. Song, S. Huang, Z. Yang, Z. J. Xu, H. Y. Yang, *Chem* **2020**, *6*, 1804.
- [15] R. Liu, Y. Wang, Y. Wu, X. Ye, W. Cai, *Electrochim. Acta* **2023**, *442*, 141815.
- [16] Z.-Y. Chen, X.-Y. Fu, L.-L. Zhang, B. Yan, X.-L. Yang, *ACS Appl. Mater. Interfaces* **2022**, *14*, 5506.
- [17] J. Liu, J. Liu, M. Tang, J. Fu, X. Kuang, J. Ma, *Adv. Funct. Mater.* **2024**, *34*, 2314167.
- [18] H. Cheng, Y. Qin, Y.-N. Liu, Z.-E. Yu, R. Li, R. Chen, J. Zhou, Y. Liu, B. Guo, *J. Mater. Chem. C* **2024**, *12*, 6785.
- [19] Y. Huang, X. Zhang, L. Ji, L. Wang, B. B. Xu, M. W. Shahzad, Y. Tang, Y. Zhu, M. Yan, G. Sun, Y. Jiang, *Energy Storage Mater.* **2023**, *58*, 1.
- [20] G. Du, H. Pang, *Energy Storage Mater.* **2021**, *36*, 387.
- [21] S. Fan, Y. Liu, Y. Gao, Y. Liu, Y. Qiao, L. Li, S. Chou, *SusMat* **2023**, *3*, 749.
- [22] J. Xiang, Y. Hao, Y. Gao, L. Ji, L. Wang, G. Sun, Y. Tang, Y. Zhu, Y. Jiang, *J. Alloy. Compd.* **2023**, *946*, 169284.
- [23] P. Xiao, J. Song, L. Wang, J. Goodenough, *Chem. Mater.* **2015**, *27*, 3763.
- [24] Y. Gao, H. Zhang, J. Peng, J. Wang, X. Liu, L. Zhang, Y. Xiao, L. Li, Y. Liu, Y. Qiao, J. Wang, S. Chou, *Adv. Mater.* **2025**, 2417876.
- [25] W. Wang, Z. Hu, Z. Yan, J. Peng, M. Chen, W. Lai, Q.-F. Gu, S.-L. Chou, H.-K. Liu, S.-X. Dou, *Energy Storage Mater.* **2020**, *30*, 42.
- [26] C. Xu, J. Peng, X. Liu, W. Lai, X. He, Z. Yang, J. Wang, Y. Qiao, L. Li, S. Chou, *Small Methods* **2022**, *6*, 2200404.
- [27] M. Jiang, Z. Hou, H. Ma, J. Wang, W. Hua, L. Ren, Y. Zhang, C. Wei, F. Kang, J. Wang, *Nano Lett.* **2023**, *23*, 10423.
- [28] Y. Gao, X. Wu, L. Wang, Y. Zhu, G. Sun, Y. Tang, M. Yan, Y. Jiang, *Adv. Funct. Mater.* **2024**, *34*, 2314860.
- [29] Y. Liu, Y. Qiao, W. Zhang, Z. Li, X. Ji, L. Miao, L. Yuan, X. Hu, Y. Huang, *Nano Energy* **2015**, *12*, 386.
- [30] Y. Moritomo, S. Urase, T. Shibata, *Electrochim. Acta* **2016**, *210*, 963.
- [31] B. Wang, S. Liu, W. Sun, Y. Tang, H. Pan, M. Yan, Y. Jiang, *ChemSusChem* **2019**, *12*, 2415.
- [32] S. Fan, Y. Gao, Y. Liu, L. Li, L. Zhang, Z. Zhou, S. Chou, X. Liu, Y. Shen, Y. Huang, *ACS Energy Lett.* **2025**, *10*, 1751.

Manuscript received: March 24, 2025

Revised manuscript received: May 9, 2025

Version of record online: